Three-dimensional mechanisms of macro-to-micro-scale transport and absorption enhancement by gut villi motions

Yanxing Wang[1,2] and James G. Brasseur[2,3]
[1]*School of Aerospace Engineering, Georgia Institute of Technology, Atlanta, GA 30332, USA*
[2]*Department of Mechanical and Nuclear Engineering, Pennsylvania State University, University Park, PA 16802, USA*
[3]*Department of Aerospace Engineering Sciences, University of Colorado Boulder, Boulder, CO 80309, USA*
(Received 3 January 2017; revised manuscript received 22 March 2017; published 19 June 2017)

We evaluate the potential for physiological control of intestinal absorption by the generation of "micromixing layers" (MMLs) induced by coordinated motions of mucosal villi coupled with lumen-scale "macro" eddying motions generated by gut motility. To this end, we apply a three-dimensional (3D) multigrid lattice-Boltzmann model of a lid-driven macroscale cavity flow with microscale fingerlike protuberances at the lower surface. Integrated with a previous 2D study of leaflike villi, we generalize to 3D the 2D mechanisms found there to enhance nutrient absorption by controlled villi motility. In three dimensions, increased lateral spacing within villi within groups that move axially with the macroeddy reduces MML strength and absorptive enhancement relative to two dimensions. However, lateral villi motions create helical 3D particle trajectories that enhance absorption rate to the level of axially moving 2D leaflike villi. The 3D enhancements are associated with interesting fundamental adjustments to 2D micro-macro-motility coordination mechanisms and imply a refined potential for physiological or pharmaceutical control of intestinal absorption.

DOI: 10.1103/PhysRevE.95.062412

I. INTRODUCTION

Absorption of nutrient and pharmaceutical molecules in the small intestines involve coupled multiscale transport and mixing processes that span several orders of magnitude. After food is ground, mixed, and released from the stomach into the duodenum, the chyme is further mixed and transported by patterned deformations of the intestinal wall (motility) at the centimeter lumen scale. The mucosa of the human intestinal wall is folded and covered with absorptive finger and leaflike protuberances called "villi" 200–400 μm in length. Each villus contains smooth muscle fibers originating within the muscularis mucosae, a thin plexus of muscle fibers and neurons under enteric neural control [1,2]. *Ex vivo* observations show that the villi move in response to external stimuli [3] and *in vivo* data suggest that villus motility might provide a unique stirring mechanism that enhances nutrient absorption at the villus epithelium [3–5]. However, due to limitations in *in vivo* experimental techniques, the details of villus motion, response to nutrient and other stimuli *in vivo*, and the potential for villi-induced enhancement of absorption are largely unknown.

Wang *et al.* [6] investigated the hypothesis that villus motility exists to *actively* enhance absorption and therefore could integrate with the neurophysiology underlying control of intestinal absorption. With a two-dimensional (2D) numerical model of planar villi within a 2D lid-driven cavity flow, they studied essential elements of gut micro-macro interactions in nutrient absorption. These results are most applicable to the 2D "leaflike" villi found along the mammalian gut mucosa. However, cylindrical "fingerlike" villi are more common and allow for more complex 3D motions than can be considered with a 2D model. In particular, whereas in 2D villi motions are necessarily axially aligned with the macroscale motions induced by the lumen-scale gut motility, the potential for 3D motion of fingerlike villi transverse to the macroscale eddies potentially creates additional mechanisms underlying enhancement and control of absorption rate.

The current study is a generalization of the 2D study in [6] to the reality of 3D motions of the more common fingerlike villi. We show that, whereas the 2D model captures essential micro-macro couplings, 3D motions create greater potential for absorption control with potentially broad applicability to gut physiology and function and opening the door to new drug-related therapies that target villi motility.

II. COMPUTATIONAL MODEL

Figure 1 illustrates the cavity-flow model in which the moving lid is used to create a macroscale eddy that *in vivo* is generated by peristaltic and segmental contractions of intestinal wall muscle with advective transport of concentrations of nutrient (and drug) molecules from the bulk to the mucosal surface for absorption. Concentration at the lid is fixed in order to model a source of molecules transported to the lower surface by a wall-driven cavity-scale eddy. In [6] the lower surface of the cavity was lined with 2D "villi" to study the potential creation of couplings between the macroscale fluid motions induced by lumen-scale motility, and the microscale motions that can be induced by villi motility—macro-micro couplings that were shown to potentially enhance the rate of transport of nutrient (and drug) molecules to the mucosal surface, and therefore absorption. Like the 2D study in [6], we model pendular motions of villi groups that have been observed *ex vivo* [3]. These controlled motions were shown in [6] to generate a "micromixing layer" (MML) that can couple with the outer macroscale eddies to enhance the rate of absorption at the lower surface in comparison with a villi-free mucosal surface. Wang *et al.* found that, contrary to the standard medical explanation for the existence of villi, the increase in epithelial surface area causes insignificant enhancement of absorption in the absence of coordinated villi motion coupled to macroscale eddying motion.

Whereas the 2D model captures essential mechanics of macro-micro interactions in the gut with laterally extended

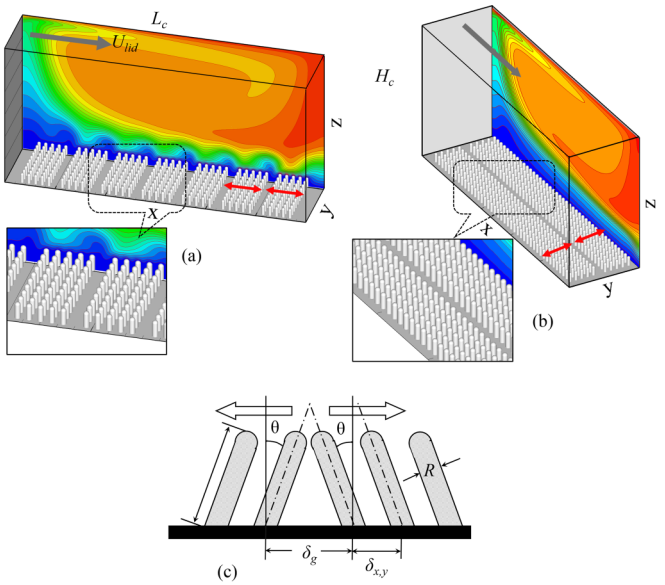

FIG. 1. The 3D model lid-driven cavity flow used to model macro-micro-scale interactions in the small intestines with (a) axial villus motion (in lid direction), and (b) lateral villus motion. Panels (a) and (b) show the groupings of villi as well as isocontours of concentration advectively driven by the macroeddy with its source at the moving upper lid (red and blue are highest and lowest concentrations, respectively). Panel (c) illustrates the specification of villus geometry and motion: (δ_x,δ_y) = distance between villi in (x,y) within groups; δ_g = distance between groups; R = villus radius. In (a) and (b) $\delta_x/R = \delta_y/R = 4$. In all simulations $\delta_g/R = 8$.

villi that move coaxially with the macroeddy motions, gut villi are 3D and tend to be "finger-shaped," with corresponding possibilities for 3D villus motion both axially and laterally *in vivo*. We here extend the 2D model to 3D to contrast the previously uncovered 2D mechanisms for absorptive enhancement with fully 3D macro-MML flow induced by coordinated axial vs lateral pendular motions of groups of cylindrically shaped villi, and to assess the impact of variable lateral villi separation. As illustrated in Fig. 1, the lower surface of the cavity is lined with moving 3D microscale fingerlike "villi" modeled as thin cylindrical protrusions with round tips in pendular motion. As in [6], the upper lid moves with constant speed to create a large-scale eddy representing luminal motions generated by gut motility. However, here we contrast axial villi motion [Fig. 1(a)] with lateral villi motion [Fig. 1(b)], coordinated within groupings of villi extended laterally using periodic boundary conditions. No-slip and zero absorption on the front and rear walls create a cavity with $L_c/H_c = 2$; absorption takes place on the lower villi-covered surface and a concentration source is generated at the moving lid. Consistent with the optimal grouping of axially moving villi found in [6], each grouping contains five villi in the axial [Fig. 1(a)] and lateral [Fig. 1(b)] directions of villus motion. In the base case, the distance between neighboring villi in the axial and lateral direction $(\delta_{x,y})$ is four times the single villus radius R ($\delta_x = \delta_y = 4R$). In all simulations villus separation in the gaps between groups is $\delta_g = 8R$ [Fig. 1(c)] with δ_g defined from villus centers.

Wang *et al.* [6] found that absorption is enhanced with sinusoidal motions of the villi tips, with each villus group oscillating 180° out of phase with its neighboring groups [Fig. 1(c)]. Nutrient molecular transport is modeled by passive scalar concentration with specified mass diffusivity D_m in water (20 °C). Numerical stability limits the Schmidt number (Sc) to ∼100, sufficiently high to contrast diffusive from advective enhancements to absorption. (Since lower diffusivity enhances the macro-micro coupling mechanisms uncovered in [6], Sc below true Sc likely produces a conservative result.) Zero-concentration boundary conditions are applied at the surfaces over and between the villi to model immediate nutrient absorption of transported molecules. Zero flux boundary conditions are applied on the front/back cavity walls with concentration =1 at the lid. No-slip velocity boundary conditions are applied on all surfaces. Periodic boundary conditions are applied across the lateral domain boundaries.

The sinusoidal displacements of the villi have specified amplitude ℓ_υ corresponding to maximum angle $\theta_{\max}$ [Fig. 1(c)]. The villus oscillating frequency f_υ (Hz) is normalized by the cavity time scale: $f_\upsilon/f_L = f_\upsilon/(U_{\rm lid}/H_c)$, where $U_{\rm lid}$ is the lid speed and H_c is the cavity height. We choose cavity characteristics consistent with the size and motility of the rat jejunum [7]: $L_c = 6\,$mm, $H_c = 3\,$mm, $U_{\rm lid} = 2\,$mm/s. However, because the rat has unusually long villi relative to lumen radius, we choose villus length $\ell_\upsilon = 200\ \mu$m as more consistent with human villi [8]. For consistency with [6], $R = 50\,\mu$m, $\theta_{\max} = 20°$, and $f_\upsilon/f_L = 40$.

To solve the flow velocities, we developed a 3D lattice-Boltzmann model (LBM) D3Q15 (see [9]) version of the 2D LBM model in [6]. The LBM equation is viewed as an explicit finite difference representation of the continuous Boltzmann equation [10]. The dependent variable is a discretized particle distribution function $f_\alpha(\mathbf{x},t)$ that quantifies the probability of finding an ensemble of molecules at discretized position $\mathbf{x}$ on a uniform square lattice at discretized time t with one of fifteen discretized velocity components $\mathbf{e}_\alpha, \alpha = 1,2,\ldots 14$ that point to neighboring nodes on the lattice, or a zero velocity at $\alpha = 0$. Macroscopic velocity $\mathbf{u}$ and density ρ are obtained from the moments of $f_\alpha(\mathbf{x},t)$. The lattice Boltzmann equation with the BGK, or Bhatnagar-Gross-Krook [9,11], representation for the collision operator is

$$f_\alpha(\mathbf{x}+\mathbf{e}_\alpha\delta t, t+\delta t) - f_\alpha(\mathbf{x},t) = -\frac{1}{\tau}[f_\alpha(\mathbf{x},t) - f_\alpha^{\rm eq}(\mathbf{x},t)], \quad (1)$$

The left-hand side (LHS) of Eq. (1) describes "streaming" the exchange of momentum between neighboring lattices as a result of bulk advection and molecular diffusion. The right-hand side (RHS) of Eq. (1) describes the mixing, or collision of molecules that drive the flow locally to the equilibrium particle distributions $f_a^{\rm eq}(\mathbf{x},t)$ with a single lattice relaxation time scale τ [9,12],

$$f_a^{\rm eq}(\mathbf{x},t) = w_a\rho(\mathbf{x},t) \times\left[1 + 3\frac{\mathbf{e}_a\cdot\mathbf{u}}{c^2} + \frac{9}{2}\frac{(\mathbf{e}_a\cdot\mathbf{u})^2}{c^4} - \frac{3}{2}\frac{(\mathbf{u}\cdot\mathbf{u})^2}{c^2}\right], \quad (2)$$

where w_α are weighting factors, $w_0 = 2/9$, $w_\alpha = 1/9$ for $\alpha = 1{-}6$ and $w_\alpha = 1/72$ for $\alpha = 7{-}14$.

We use passive scalar concentration $\phi(\mathbf{x},t)$ to model the transport and absorption of nutrient molecules at the continuum level, and solve for $\phi(\mathbf{x},t)$ using the "moment propagation method" developed by Frenkel and Ernst [13], Lowe and Frenkel [14], and Merks *et al.* [15], in which $\phi(\mathbf{x},t)$ is propagated along with the particle distribution function $f_\alpha(\mathbf{x},t)$ as

$$\phi(\mathbf{x},t+\delta t)=\sum_\alpha P_\alpha(\mathbf{x}-\mathbf{e}_\alpha\delta t,t+\delta t)+\Delta^*\phi(\mathbf{x},t), \quad (3)$$

and

$$P_\alpha(\mathbf{x}-\mathbf{e}_\alpha\delta t,t+\delta t) = \left[\frac{\hat{f}_\alpha(\mathbf{x}-\mathbf{e}_\alpha\delta t,t_+)}{\rho(\mathbf{x}-\mathbf{e}_\alpha\delta t,t)}-w_\alpha\Delta^*\right]\phi(\mathbf{x}-\mathbf{e}_\alpha\delta t,t), \quad (4)$$

where

$$\Delta^*=1-6\frac{D_m}{c\delta x}. \quad (5)$$

D_m is the mass diffusivity, c is the lattice speed, and δx is lattice spacing. Zero scalar boundary conditions are applied on the lower surface of the cavity and in between villi surfaces to model the limit of immediate absorption. Fixed scalar =1 was applied at the lid to model a scalar source in the bulk fluid within the intestinal lumen, and zero flux scalar boundary conditions were applied on the side walls of the cavity.

To resolve the microscale villi-driven flow with a lattice finer than the macroscale outer flow, we apply the multigrid strategy developed by Filippova and Hanel [16] and Yu *et al.* [17]. The transfer of distribution functions across the interface between the coarse and fine grids is performed according to the conservation of mass and continuity of stresses. See Wang *et al.* [18] for LBM details and accuracy analysis.

All quantifications were carried out in the stationary state, when time averages over a villus oscillation period are time independent. In this stationary state the streamlines within the time averaged velocity field are equivalent to the time-averaged trajectories of fluid particles. In what follows we contrast absorption associated with axial motion of the 3D fingerlike villi with the 2D analysis in [6]. We then analyze absorption with lateral motions of villi groups within an axial macroscale eddy, creating 3D flow at the microscale.

III. RESULTS AND DISCUSSION

Figures 1(a) and 2–4 summarize the results of our 3D study with axial oscillatory motions of laterally extended villi groups, that is, villi motion in the same direction as the fluid motions induced by the macroscale eddy. These results are discussed next (Sec. III A) where we contrast axial motions of fingerlike villi with absorption enhancement physics associated with the 2D axial motions of 2D villi reported in [6]. We follow in Sec. III B by contrasting the 2D and 3D coupling mechanisms associated axially moving villi with the 3D fluid mixing motions that are induced by villi groups moving laterally to the macroscale eddy flow. The advances in knowledge are summarized in context with the key results presented in Figs. 1(b) and 5–7.

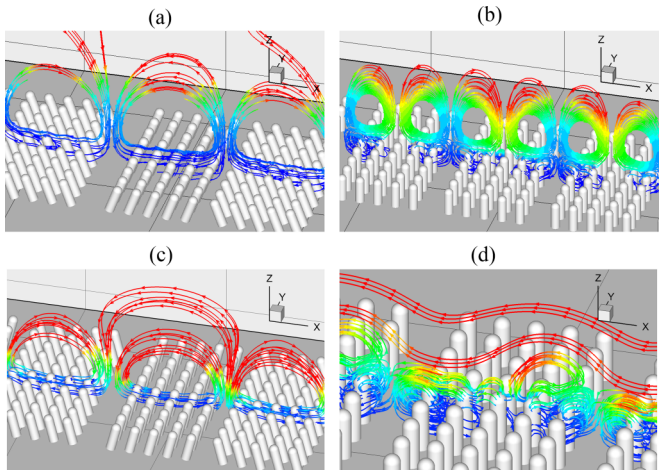

FIG. 2. Cavity flow with *fixed* lid is shown in (a) with instantaneous streamlines and (b) with time-averaged streamlines. The same cavity flow with *moving* lid is shown in (c) with instantaneous streamlines and (d) with time-averaged streamlines. Time averaging is over a single period in the stationary state; time-averaged particle paths coincide with time-averaged streamlines. The perspective in (d) focuses on the 3D structure of the time-averaged surface streamlines within vs above the villi. Streamlines are colored with scalar concentration (dark red = local maximum; dark blue = zero). $\delta_x/R=\delta_y/R=4$.

A. Axial villi motion

The essential macro-micro-coupling mechanisms uncovered in the 2D study [6] are found to also underlie absorption enhancement with axially moving 3D fingerlike villi, with

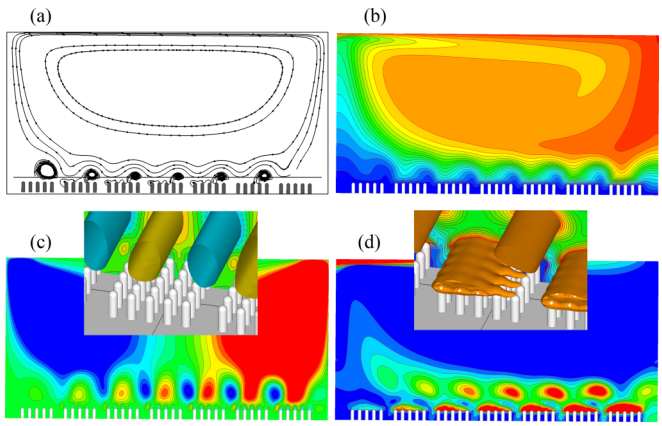

FIG. 3. Variables averaged over a period in the stationary state. Panel (a) shows the time-averaged streamline (and particle path) pattern over the cavity [Fig. 2(d) shows a blown-up view at the villi], and (b) shows the time-averaged concentration field. Panels (c) and (d) show contributions to the vertical concentration flux balance: (c) shows advective flux $-\overline{u_z\phi}$ and (d) shows diffusive flux $\overline{D_m\partial\phi/\partial z}$, where ϕ is the concentration field and z is the vertical coordinate. The insets show isosurfaces at fixed flux values, illustrating the quasi-2D nature of the scalar field and flow field above the villi groups. Colors: in (b) red = 1, blue = 0; in (c) the red and blue isocontours show maximum local time-averaged flux toward the villi ($-z$) and towards the lid ($+z$), respectively ($\pm1\times10^{-4}$ m/s, green $\approx$ zero); in (d) all diffusive flux is towards the villi: red $=2\times10^{-5}$ m/s, blue $=2\times10^{-6}$ m/s. $\overline{\beta}\Rightarrow$ time averaged β. $\delta_x/R=\delta_y/R=4$.

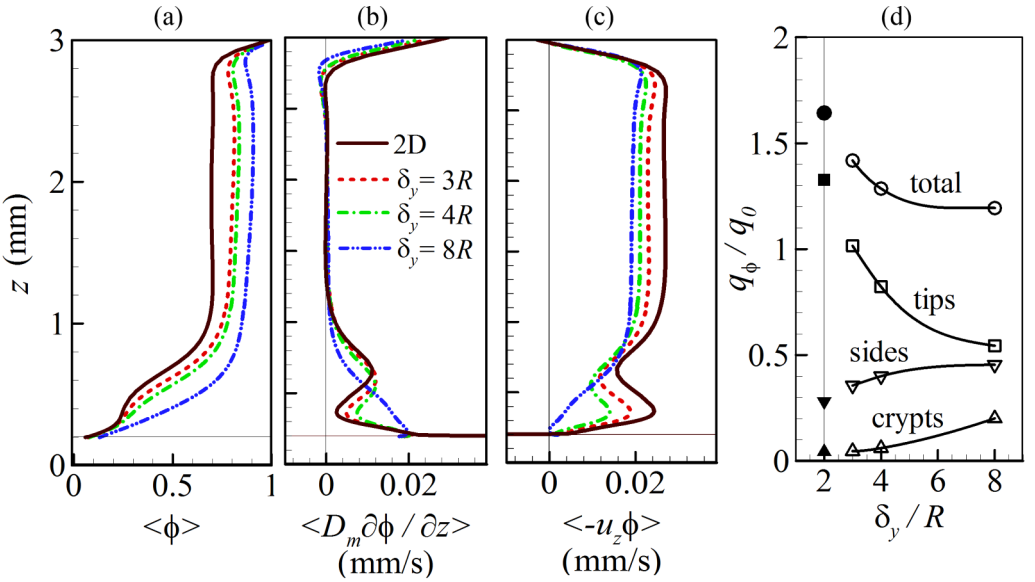

FIG. 4. Space-time averaged (a) scalar concentration, (b) diffusive flux, and (c) advective flux as a function of lateral villi spacing δ_y. Panel (d) shows absorption rate as a function of δ_y/R; q_0 = net flux without villi. The 2D result [6] is given at $\delta_y/R = 2$. $\langle\rangle \Rightarrow$ average on z planes. ϕ is unitless. In all simulations $\delta_x/R = 4$.

important differences associated with the 3D nature of the flow around individual villi. Figures 2(a) and 2(b) show the microscale flow with fixed lid, i.e., without the lid-driven outer eddy. The instantaneous streamlines in Fig. 2(a) show fluid ejected *from* the closing gaps between villi groups and returning *into* the opening gap regions—the generation of a "micromixing layer" (MML) in the instantaneous flow field driven by the counteroscillating villi groups. However, Fig. 2(b) shows that in the stationary state the *time-averaged* MML is pumped from *all* gap regions and returns symmetrically to the centers of the villi groups. The time-averaged trajectories of fluid particles coincide with these average streamlines. The streamlines in Fig. 2 are colored by local concentration; thus, as fluid particles are pumped from the gaps they carry with them low-concentration fluid and return to the villi tips at higher concentration. With no macroscale eddy, scalar transport from the lid to the fluid particles at the upper margin of MML is purely diffusive. Locally near the lower surface, mixing is enhanced, with corresponding modest enhancement of net surface scalar flux driven by a MML that scales on the width and oscillatory velocity of the villi groups.

However, much greater enhancement results from the coupling of micro- and macroscale motions. Figure 2(c) shows instantaneous streamlines that, like the case without an outer eddy, proceed from converging villi gaps to the gaps with diverging villi. However, Fig. 2(d) shows that, on average, the presence of an outer macroeddy removes symmetry in the time-averaged streamline pattern of the villi-induced MML and reduces the vertical scale of the MML. Again, fluid particles are pumped, on average, from all gaps at low concentration to the lower margins of the macroeddy and return at higher concentration to the top of the adjacent villi group. However, the clockwise-rotating microeddy is suppressed and fluid particles travel, on average, asymmetrically over a larger area of villi tips, increasing the absorption area and absorption rate. This was found also to be the case with the 2D model [6]. The creation of the eddying structure of the MML is a manifestation of the disparate micro villi scale to the macroeddy scale, here induced by a moving lid but *in vivo* a result of intestinal motility at the lumen scale.

Plots of time-averaged variables over the cavity in Fig. 3 show a micro-macro handshake between advective and diffusive transport similar to that found in two dimensions. Figures 3(a) and 3(b) show the time-averaged streamline pattern and concentration field. As was shown in the close-up streamline view of Fig. 2(d), symmetry breaking in the local streamline pattern near the villi tips by the macroeddy causes the MML fluid particles, driven vertically from the gaps to the lower margins of the macroeddy [Fig. 3(a)], to be driven back down over broad areas of the villi tips. Figure 3(b) shows that fluid particles driven from the gaps are depleted of nutrient molecules while fluid particles driven toward the villi surfaces are at much higher concentration,

The basic mechanism is shown in Figs. 3(c) and 3(d), where the advective and diffusive contributions to the time-averaged scalar flux balance are plotted. Comparing advective flux in Fig. 3(c) with diffusive flux in Fig. 3(d), we see that advective flux dominates in the outer macroeddy flow to transport molecules from the lid to the villi (red), and in the microscale MML flow to transport molecules from the lower margins of the macroeddy to the villi surface (local red regions) and from the gaps to the macroeddy (local blue regions). The red isocontours in Fig. 3(d) show high diffusive flux in localized regions that separate the MML from the macroeddy, allowing fluid particles in the upper MML to rapidly absorb nutrient molecules from the lower margins of the nutrient-rich macroeddy before returning to the villi tips, where they are diffusively absorbed [Fig. 3(d), red at villi tips].

Enhanced absorption is associated with the path taken by fluid particles by this macro-micro handshake [6]. As shown in Fig. 2(d), on average fluid particles are ejected at low concentration from between counteroscillating villi groups

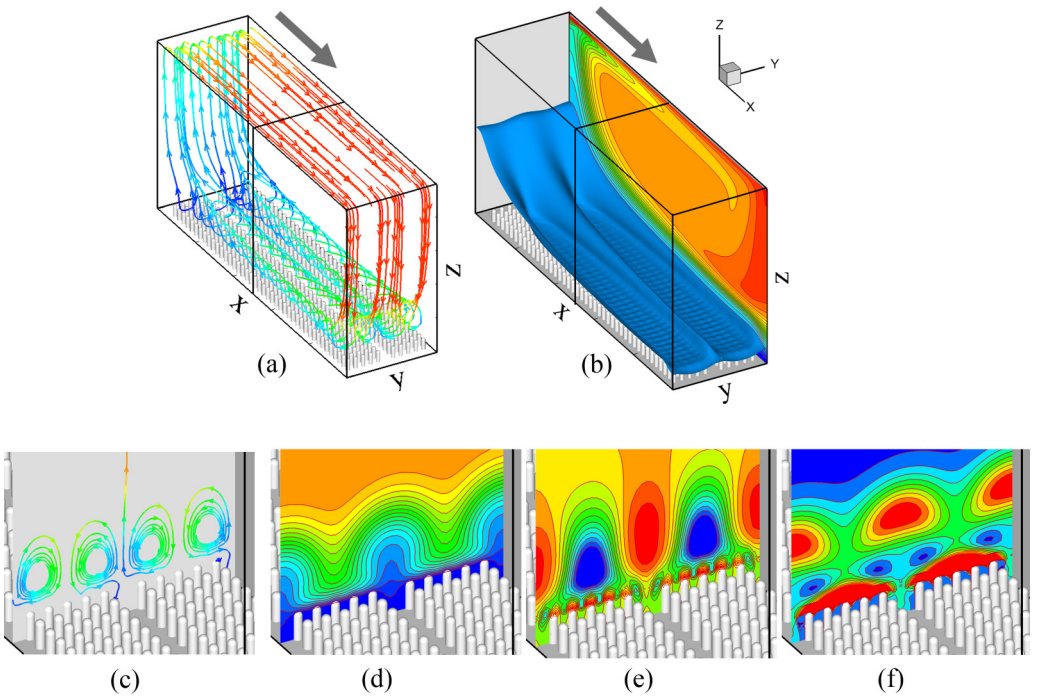

FIG. 5. Time-averaged flow fields with transverse villus motion with moving cavity lid. (a) 3D streamlines (and time-averaged particle paths); (b) isocontours and a single isosurface ($\bar{\phi} = 0.2$) of concentration; panels (c)–(f) show the following on the lateral plane midway in the cavity ($x = L_c/2$): (c) projected streamlines colored by concentration, (d) isocontours of concentration (red = 1, darkblue = 0), (e) vertical concentration flux by advection (where red is max upwards and dark blue is max downwards flux), and (f) flux by diffusion (where red is maximum downwards and blue is ≈ zero). $\delta_x/R = \delta_y/R = 4$.

and are transported to the upper MML where nutrient-rich molecules are absorbed diffusively from the macroeddy that has advectively transported molecules downward from the lid to the upper MML. These high-concentration fluid particles are then transported within the MML to the villi tips where they are absorbed [Fig. 3(d)]. Absorptive surface area is enhanced by asymmetry induced in the streamline pattern by macro-micro interaction [Fig. 2(d)]. The time-averaged fluxes are quasi-2D in nature [inset images of Figs. 3(c) and 3(d)], suggesting that three-dimensional modulations are largely from 3D flow between villi legs and in the gaps between villi groups [Fig. 2(d)].

When the time-averaged fluxes shown in Fig. 3 are also averaged on horizontal planes, the sum produces *net flux* q_ϕ that is independent of z:

$$\left\langle \overline{D_m \frac{\partial \phi}{\partial z}} \right\rangle (z) + \langle -\overline{u_z \phi} \rangle (z) = q_\phi, \tag{6}$$

where the overbar indicates time average and the brackets imply averaging over lateral cavity area. 3D vs 2D space-time-averaged advective and diffusive fluxes, with concentration profile, are plotted in Figs. 4(a)–4(c). Figure 4(d) quantifies the enhancement of absorption rate q_ϕ relative to the flux that would exist without villi (q_0) with relative contributions from villi tips, sides, and "crypts" (lower surface between villi), plotted with varying lateral spacing δ_y/R between villi. Figure 4(d) shows that when the villi are tightly packed ($\delta_y/R = 3$), enhancement of absorption is lower by 22% with 3D fingerlike vs 2D villi, largely due to reduced pumping in the gaps. In this *in vivo* scenario [3], the tips provide most of the total absorption (77–80% with finger or 2D villi). The sides provide from 25% to 18% with tightly packed finger or 2D villi to 38% at large lateral spacing. We conclude that, even with lower pumping strength of 3D vs 2D MMLs, the 3D nature of the flow and absorption on the villi sides maintains potentially strong enhancements to absorption by controlled grouped villi motions (42% enhancement in three dimensions; 64% in two dimensions). Figures 4(b) and 4(c) show that the "layering" between advective and diffusive flux—described above as underlying the enhancement of absorption by villi motility—is strong with lateral spacing up to $\delta_y/R = 4$, but largely disappears at $\delta_y/R = 8$. Similarly, the mixing-induced uniform space-time-averaged concentration within the MML disappears when $\delta_y/R = 8$ [Fig. 4(a)].

We conclude that in both the current 3D and previous 2D analysis when villi move coaxially with macroeddying motions, underlying the enhancement of nutrient absorption is a handshake that takes place between advective and diffusive transport. Advective transport moves nutrient molecules from higher concentration above within the macroscale eddy at the macroeddy time scale which, for Peclet numbers >1 is more efficient than diffusion. However, additional enhancement derives from the existence of a specific villous-driven MML, where diffusive transport at the interface between the MML and macroeddy couples with advective transport within the MML (at the same time scale) to enhance the net transport of nutrient molecules to the villi surface where it is diffusively absorbed. The strength of this basic handshaking mechanism is modulated by the degree of spacing between villi within the villi groups.

B. Lateral villi motion

In the above we considered villi-driven motions axially aligned with the macroscale eddy characterizing lumen-scale motility *in vivo*. However, the villi can move in three dimensions with mixes of axial and lateral motion. In Figs. 1(b) and 5–7 we analyze the limit of purely lateral villi motion perpendicular to the lid-driven eddy, with $\delta_x/R = \delta_y/R = 4$. Figure 5 shows the patterns of the macro-micro-scale interaction with lateral villus motion. In Fig. 2(b) above we showed that when the villi move axially without a lid-driven macroflow, time-averaged counter-rotating microeddies are created over each villus group in the direction of villus motion. This is also the case in the direction of villi motion when the villi move laterally in the presence of a lid-driven macroeddy as shown by the projected 3D streamlines in Fig. 5(c); in the time average, fluid leaves the axially aligned gaps from two counter-rotating groups of villi; Fig. 5(d) shows that the fluid particles leaving the gaps are depleted of scalar concentration. As shown by the colored streamlines in Fig. 5(c), the fluid particles travel vertically where they collect concentration from the lower margin of the outer eddies before returning to the tips of the villi in the middle of the villi groups at much higher concentration than when they left the gaps.

Since the macroeddy motions act perpendicular to villi motion, symmetry in the lateral microeddy structure is not broken as it was with axially aligned micro-macro flows [Fig. 2(d)] enhancing the surface area for absorption. However the axially aligned macroscale motions force the MML microscale streamlines into a helical pattern [Fig. 5(a)] providing another mechanism for enhancing the surface area for absorption into villi tips from high-concentration fluid particles returning to the villi. The streamline pattern in Figs. 5(a) and 5(c) together with scalar concentration [Fig. 5(d)] and the layering of advective and diffusive vertical scalar flux in Figs. 5(e) and 5(f) demonstrate the interaction between microscale eddies in the MML and the macroeddy to enhance scalar flux. Like axially driven villi, the MML acquires molecules from the macroeddy via the molecular diffusion layer above [Fig. 5(f)] and advects this higher-concentration fluid to the villi tips for absorption through a diffusion layer below [Fig. 5(e)]. Micro-macro interactions force the MML streamlines into helical patterns that enhance absorptive surface area.

The highly three-dimensional transition between the laterally driven flow within the laterally moving villi and the axial macroeddy flow driven by the moving lid is shown in Fig. 6 through the 3D time-averaged streamline pattern. We observe relatively abrupt transitions between a largely lateral small-scale flow pattern around the villi legs and a largely axial large-scale flow pattern in the external macroeddy. The transition between the macroscale outer eddy and the flow within the villi is a highly helical pattern that defines the average structure of the MML flow. This streamline pattern is a result of fluid particles being driven axially from above and laterally from below. As shown in Fig. 6(b), the axial forcing from the macroscale flow from above also manifests within the villi by a slow axial contribution to the mostly lateral flow that forces the fluid particles around the sides of the villi in more highly 3D fashion than in the case of axial villi motion [compare Figs. 2(d) and 6]. This axial flow within the villi

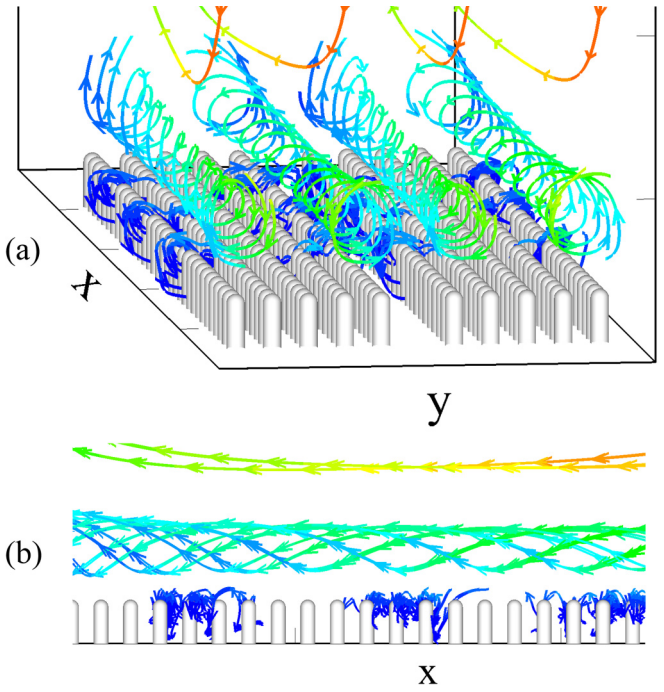

FIG. 6. Time-averaged 3D streamline and particle path patterns displaying the three-layer structure of the three-dimensional MML when villi groups move laterally to the macroeddy flow, displayed. (a) Perspective view; (b) side view. The streamlines are colored by scalar concentration consistent with the colors in Figs. 5(b) and 5(d).

legs likely contributes to an enhancement of absorption into the villi legs.

In Fig. 7(a) we quantitatively compare enhancement of absorption and macro-micro-scale interactions created by axial vs lateral villi motion with averaging over horizontal planes and time (see Fig. 4). Net flux is increased by 25% when the villi move laterally vs axially ($q_\phi/q_0 = 1.60$ lateral vs 1.28 axial). In fact, lateral motion of fingerlike villi produced absorption enhancement comparable to 2D flow with laterally extended 2D villi ($q_\phi/q_0 = 1.64$). Figure 7(a) shows that increased absorption enhancement results largely from increased advective transport in the MML—nearly twice as high with lateral vs axial villi motion. The greatest increase in absorption enhancement is at the villi tips (29%) and sides (22%).

To understand better the mechanisms that underlie the improved enhancement of absorption with lateral villi motion, we plot in Figs. 7(b) and 7(c) time-averaged vertical velocity u_z and scalar concentration along axial lines above the villi tips at the height of advective enhancement [Fig. 7(a)]. The solid red curves quantify lateral villi motion variables above the group center and above gaps between villi groups (see Fig. 1). The dashed blue curves quantify axial villi motion variables along arbitrary axial lines above villi. The sinusoidal variations reflect transition between villi group centers and gaps. A similar sinusoidal variation occurs in the lateral direction with lateral villi motion; the upper and lower solid curves in Figs. 7(b) and 7(c) are the maxima and minima of this lateral oscillatory behavior. Thus Fig. 7(b) shows that over the centers of the villi groups and over the gaps the vertical

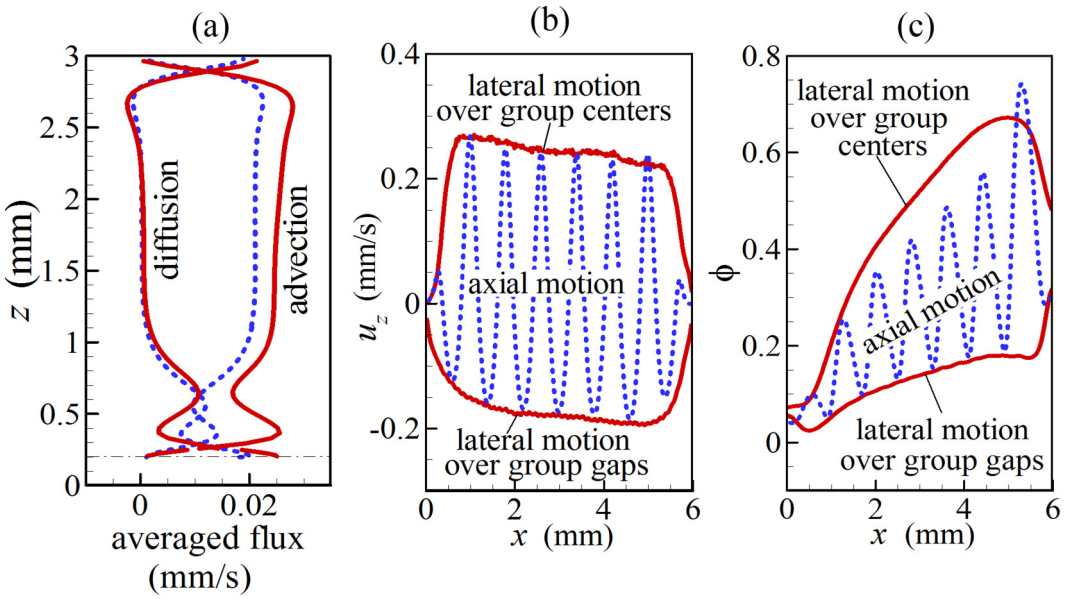

FIG. 7. Comparison of MMLs generated by lateral (red, solid curves) vs axial (blue, dashed curves) villus motion. (a) Space-time-averaged vertical scalar flux by advection and diffusion (as indicated). (b), (c) Axial distributions of time-averaged (b) vertical velocity and (c) scalar concentration along axially drawn lines at $z = 0.35$ mm. With axial motion these are along arbitrary lines in x [see Fig. 1(a)]. With lateral villi motion these are over villi group centers and over gaps in between the villi groups, as indicated [see Fig. 1(b)]. $\delta_x/R = \delta_y/R = 4$.

velocity u_z is the same for axial and lateral villi motion. That is *not* the case with scalar concentration ϕ [Fig. 7(c)]: ϕ is the same for axial vs lateral villi motions only over the gaps. Over the centers of the villi groups in the advection-dominated region of the MML, scalar concentration is much higher with lateral motion, creating higher advective flux to the villi and increased absorption.

We may speculate as to mechanisms. Comparing the isosurface in Fig. 5(b) with the streamline pattern of Figs. 5(a), 5(c), and 6 suggests that the helical streamline structure induced by micro-macro interactions underlies high concentration axially along the villi group centers and effective absorptive surface area. It appears that lateral oscillatory motions of coordinated villi groups axially extended are more effective at transporting high concentration fluid over larger villi tip areas than with axial oscillatory motions where the effective area increase is reduced by the gaps between villi groups.

IV. CONCLUDING REMARKS

We have found in this study that the essential mechanisms deduced from the 2D lid-driven cavity flow model apply to the more realistic three-dimensional villus finger model when the 2D and 3D villus groups both move in the same direction as the external macroscale flow driven, *in vivo*, by motility at the gut lumen scale. It is not surprising to also find, however, that the strength of the MML, and therefore also the absorption rate, reduces as the lateral spacing between villi increases. The reduction is somewhat mitigated by the enhancement of absorption by 3D flow around the villi legs, but is significant. Therefore it is interesting to observe that the highly three-dimensional flow generated by oscillatory motion of villi groups in directions perpendicular to the macroeddy flow leads to enhanced absorption to the same level as the fully axial 2D macro-micro flows resulting from the interaction between leaflike villi infinitely extended in the lateral direction and the macromotility-induced large-scale eddying motions. This greater enhancement of absorption is a direct consequence of the spatially rapid changes in flow structure between microscale villi-induced and macroscale motility-induced motions that generates a helical micromixing layer structure—a highly 3D microscale flow that even more effectively couples the advective transport of nutrients from the macroscale eddy with advective transport within the helical microscale eddy across a diffusion-dominated interface. While the mechanical mechanisms with lateral villi motion are similar to the case with axially moving villi, the enhancement of nutrient transport is more effective when the villi oscillate in directions perpendicular to the macroeddy flow due to the enhanced effective absorptive surface area induced by the helical MML pattern over axially extended villi groups [Fig. 5(c)].

The results of the current study may have broad implications. Although intestinal absorption relies on mixing with acidic gastric and duodenal pancreatic and bile secretions generated by lumen-scale contractions of the muscularis propria, these motions are insufficient for digestion at the physiological time scale [4]. Our studies have shown that couplings with coordinated microscale motility of the villi that line the gut mucosa provide potential enhancement mechanisms. Furthermore, because villi motility is enterically stimulated, villi-induced enhancement of absorption can be locally controlled. This local enterically controlled micro-macro-coupling mechanism might be pharmaceutically exploited through drugs [19] specifically designed to modulate villus motility, and therefore absorption. The micro-macro-coupling mechanisms uncovered here might also be applied to other mixing processes in low Reynolds number flow environments.

ACKNOWLEDGMENTS

We gratefully acknowledge support from the U.S. National Science Foundation under Grant No. CTS 056215. This research program was within the Microscale Modeling (MSM) consortium under the multiagency Interagency Modeling and Analysis Group (IMAG) that spanned the following U.S. funding agencies: NIH, NSF, NASA, DOE, DOD, and USDA.

[1] J. M. DeSesso and C. F. Jacobson, Food Chem. Toxicol. **39**, 209 (2001).
[2] J. D. Wood, Gastroenterology **127**, 635 (2004).
[3] W. A. Womack, P. R. Kvietys, and D. N. Granger, in *Handbook of Physiology*, edited by J. D. Wood, S. G. Schultz, and B. B. Rauner (American Physiological Society, Bethesda, 1989), p. 975.
[4] M. D. Levitt, A. Strocchi, and D. G. Levitt, Am. J. Physiol. **262**, G593 (1992).
[5] A. Strocchi, G. Corazza, J. Furne, C. Fine, A. D. Sario, G. Gasbarrini, and M. D. Levitt, Am. J. Physiol. **270**, G487 (1996).
[6] Y. Wang, J. G. Brasseur, G. G. Banco, A. G. Webb, A. C. Ailiani, and T. Neuberger, Philos. Trans. R. Soc. A **368**, 2863 (2010).
[7] A. C. Ailiani, T. Neuberger, J. G. Brasseur, G. Banco, Y. Wang, N. B. Smith, and A. G. Webb, Mag. Reson. Med. **62**, 116 (2009).
[8] J. L. Z. Infante, J. M. Rouanet, and P. Besancon, Gut **34**, 1066 (1993).
[9] S. Chen and G. D. Doolen, Annu. Rev. Fluid Mech. **30**, 329 (1998).
[10] X. Shan, X. Yuan, and H. Chen, J. Fluid Mech. **550**, 413 (2006).
[11] P. L. Bhatnagar, E. P. Gross, and M. Krook, Phys. Rev. **94**, 511 (1954).
[12] Y. Qian, D. d'Humieres, and P. Lallemand, Europhys. Lett. **17**, 479 (1992).
[13] D. Frenkel and M. H. Ernst, Phys. Rev. Lett. **63**, 2165 (1989).
[14] C. P. Lowe and D. Frenkel, Physica A **220**, 251 (1995).
[15] R. M. H. Merks, A. G. Hoekstra, and P. M. A. Sloot, J. Comput. Phys. **183**, 563 (2002).
[16] O. Filippova and D. Hanel, J. Comput. Phys. **147**, 219 (1998).
[17] D. Yu, R. Mei, L. Luo, and W. Shyy, Int. J. Num. Meth. Fluids **39**, 99 (2002).
[18] Y. Wang, J. G. Brasseur, G. G. Banco, A. G. Webb, A. C. Ailiani, and T. Neuberger, in *Computational Modeling in Biomechanics* (Springer, Heidelberg, 2010), p. 69.
[19] E. Kokas and H. A. Gordon, J. Pharmacol. Exp. Ther. **180**, 56 (1972).